Geophys. J. Int. (2009) **178,** 623–637 doi: 10.1111/j.1365-246X.2009.04188.x

A comprehensive study of including structural orientation information in geophysical inversions

Peter G. Lelièvre and Douglas W. Oldenburg

UBC-Geophysical Inversion Facility, Department of Earth and Ocean Sciences, University of British Columbia, Vancouver, BC, V6T 1Z4, *Canada.*
E-mail: plelievre@eos.ubc.ca

Accepted 2009 March 19. Received 2009 March 19; in original form 2008 September 30

SUMMARY

In this paper, we investigate options for incorporating structural orientation information into under-determined inversions in a deterministic framework (i.e. minimization of an objective function). The first approach involves a rotation of an orthogonal system of smoothness operators, for which there are some important practical details in the implementation that avoid asymmetric inversion results. The second approach relies on addition of linear constraints into the optimization problem, which is solved using a logarithmic barrier method. A 2-D synthetic example is provided involving a synclinal magnetic structure and we invert two sets of real survey data in 3-D (one gravity data, the other magnetic data). Using those examples, we demonstrate how different types of orientation information can be incorporated into inversions. Incorporating orientation information can yield bodies that have expected aspect ratios and axis orientations. Physical property increase or decrease in particular directions can also be obtained.

Key words: Inverse theory; Gravity anomalies and Earth structure; Magnetic anomalies: modelling and interpretation.

1 INTRODUCTION

To be reliable, earth models used for mineral exploration should be consistent with all available geophysical and geological information. Due to data uncertainty and other aspects inherent to the under-determined geophysical inverse problem, there are an infinite number of models that can fit the geophysical data to the desired degree (i.e. the problem is non-unique). Further information is essential for a unique solution. Incorporating prior geological knowledge can reduce ambiguity and enhance inversion results, leading to more reliable earth models.

An important form of available geological information is structural orientation. This can involve the orientation of a body (i.e. the strike, dip, and tilt of its major axes), aspect ratios (i.e. the relative lengths of a body's major axes) and physical property trends (i.e. increase, decrease, or constant in a particular direction). The ability to specify such information becomes especially important for survey methods with limited depth resolution. The lack of resolution can lead to recovery of an object with an incorrect or distorted dip and by including orientation information the results can be dramatically improved at depth.

Many researchers have provided functionality for incorporating different types of geological information into their particular inversion frameworks. In this paper, we investigate how orientation information can be placed into our deterministic inversion framework in which a computationally well-behaved function is minimized subject to optional constraints. Before introducing our methods we provide an overview of some techniques used by other authors for comparison.

Bosch *et al.* (2001) and Guillen *et al.* (2008) work in a stochastic inversion framework that directly recovers rock type (i.e. a lithologic inversion) from a list of those assumed present. Prior information is placed into the problem through probability density functions and topology rules (relationships between rock units). The model space (i.e. all possible models) is investigated (sampled) through a random walk process, an approach proposed by Mosegaard & Tarantola (2002). This strategy provides not only model estimates but also statistical information regarding the model space. In contrast to the functions in our deterministic framework, their probability density functions and structural topology measures are not required to be differentiable, and hence, there is more flexibility in the types of geological information that can be incorporated. However, their approach relies on random sampling methods that lead to much heavier computational costs than deterministic approaches.

Chasseriau & Chouteau (2003) introduce regularization through a parameter covariance matrix, the elements of which are estimated statistically using variograms. The covariance matrix can be estimated from physical property data (e.g. measurements taken at surface or down drill-holes) or using some initial model(s) representing the best guess at the subsurface distribution. The variogram calculations involve three specified ellipsoid axes in any spatial directions and as such, their method allows construction of structures with different shapes and orientations. Estimation of the covariance parameter matrix requires significant memory and computation time.

Last & Kubik (1983) developed a compact (minimum volume) gravity inversion. Guillen & Menichetti (1984) extended the method to allow specification of a dip line along which the moment of inertia is minimized. Barbosa *et al.* (1994) extended the method further to allow specification of mass concentration information along several arbitrary axes. The compactness measures used lead to non-linear functions to be minimized (in a deterministic framework) or sampled, (in a probabilistic framework) which increases the computational burden above that of our methods.

Barbosa & Silva (2006) apply the method of Barbosa *et al.* (1994) within an interactive environment in which the interpreter can adjust the arbitrary axes as desired to aid geological hypothesis testing. As such, their approach is similar to interactive forward modelling, where the interpreter investigates the model space, but differs in that the algorithm automatically fits the data.

Another novel approach is that of Wijns & Kowalczyk (2007) who, similarly to the approach of Barbosa & Silva (2006), allow for input from the interpreter to help ensure a geologically reasonable solution. Several inversions are performed with random values for several control parameters. The resulting suite of recovered models are then visually inspected by the interpreter and ranked by how geologically reasonable they are (based on the interpreter's prior knowledge). A genetic algorithm then takes that ranking into account and modifies the control parameter set to generate a new suite of models. This procedure progressively converges towards a reasonable set of solutions but requires a significant increase in the amount of inversions performed.

Orientation information can be incorporated in a natural way into all of the methods mentioned above. There is significant computational cost associated with most of those and we choose to work in a relatively computationally efficient deterministic framework.

Orientation information may come in different forms. Surface mapping can provide direct local measurements of structural orientation. Additional drilling may indicate approximate orientation information across larger volumes. If a geological (rock) model can be created in the later stages of exploration then this can provide orientation information everywhere within the volume. Such information can be placed into an inversion as so-called 'soft' or 'hard' constraints, the former being a request and the latter being a guarantee. We begin by presenting soft and hard approaches for incorporating orientation information into our inversion framework. Then we demonstrate the use of our methods on scenarios involving different types of orientation information.

2 INCORPORATING ORIENTATION INFORMATION AS SOFT CONSTRAINTS

2.1 Our deterministic inversion framework

In our numerical inverse solutions, the earth region of interest is divided into many cells within an orthogonal mesh with the physical property of interest being constant across each cell. There are generally more cells than there are data and the resulting underdetermined inverse problem is formulated as an optimization that involves minimization of a (total) objective function, Φ, that combines a data misfit measure, Φ_d, with a regularization term, Φ_m, also called the model objective function:

$$\min_{\mathbf{m}} \quad \Phi(\mathbf{m}) = \Phi_d(\mathbf{m}) + \beta\Phi_m(\mathbf{m}), \tag{1}$$

where $\mathbf{m}$ is the model vector that holds the physical property values in each mesh cell of our discretized earth; β is a trade-off parameter that controls the relative size of the Φ_d and Φ_m measures for the resulting model and allows us to tune the level of data fit as desired. The data misfit term controls how well we fit the data and the regularization term allows us to control the amount and type of structure in the recovered model.

The data misfit term measures the difference between the noisy observed data, $\mathbf{d}^{\text{obs}}$, and the data produced (predicted) by a candidate model, $\mathbf{d}^{\text{pred}} = F[\mathbf{m}]$. We define the data misfit as a sum-of-squares

$$\Phi_d = \sum_{i=1}^{N} \left(\frac{d_i^{\text{pred}} - d_i^{\text{obs}}}{\sigma_i} \right)^2, \tag{2}$$

where N is the number of data. Each data difference is normalized by an uncertainty, σ_i. These uncertainties are estimated errors in the observed data. The larger the uncertainty in an observed datum, the smaller its contribution to the misfit measure.

We use a model objective function that helps to recover smooth physical property models. Li & Oldenburg (1996) developed a model objective function that measured smoothness in three axial directions, with tunable parameters allowing specification of different elongations along those axes. Li & Oldenburg (2000) extended this formulation to allow the three axes to be arbitrarily rotated in 3-D, thereby, allowing inclusion of important orientation information (strike, dip, and tilt) into the inversion in a soft manner. Below we provide a brief synopsis of the method of Li & Oldenburg (2000) and we demonstrate some drawbacks of, and our improvements to, their implementation.

2.2 Specifying preferred elongation directions and aspect ratios

Li & Oldenburg (1996) designed a model objective function of the following form:

$$\begin{aligned}\phi_m(m) = &\int_V w_s\left(m - m_{\text{ref}}\right)^2 dv \\ &+ \int_V w_x \left\{ \frac{\partial}{\partial x}\left(m - m_{\text{ref}}\right) \right\}^2 dv \\ &+ \int_V w_y \left\{ \frac{\partial}{\partial y}\left(m - m_{\text{ref}}\right) \right\}^2 dv \\ &+ \int_V w_z \left\{ \frac{\partial}{\partial z}\left(m - m_{\text{ref}}\right) \right\}^2 dv. \end{aligned}\tag{3}$$

(we use ϕ and m for continuous space and Φ and $\mathbf{m}$ for the discrete case). By altering the relative values of the smoothness weights w_x, w_y, and w_z in eq. (3) we can cause the recovered models to become smoother (i.e. elongated) in some mesh-orthogonal direction(s) compared to the other(s), allowing specification of relative aspect ratios.

Specifying a preferred elongation in any (generally non-axial) direction is not possible using eq. (3) because the derivatives are squared and directional information is, thereby, lost (Li & Oldenburg 2000). In general, the geological features will not be aligned with the mesh axes because the mesh is designed such that its horizontal axes are compatible with the survey grid over which the data were collected (with the remaining axis vertical).

2.3 A two-dimensional dipping model objective function

A further generalization of the model objective function by Li & Oldenburg (2000) allows the coordinate axes to be rotated such

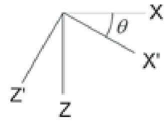

Figure 1. The mesh-orthogonal and rotated coordinate systems for a 2-D problem.

that preferred elongations can be specified in any directions. Below, we summarize their formulation for the 2-D problem. The mesh-orthogonal axes are denoted x and z with the x-axis horizontal and z positive down. The rotated coordinates are x' and z'. The dip angle between the two coordinate systems is θ, measured downward from horizontal (i.e. from the x-axis towards the z-axis). This is represented graphically in Fig. 1. The angle θ is used to align the rotated coordinates with the principal axes of the subsurface structures.

The new model objective function in 2-D, with smoothness directions specified by the rotated axes, is

$$\phi_m(m) = \int_V w_s\left(m - m_{\text{ref}}\right)^2 dv + \int_V w_{x'}\left(\frac{\partial m}{\partial x'}\right)^2 dv + \int_V w_{z'}\left(\frac{\partial m}{\partial z'}\right)^2 dv, \quad (4)$$

where we have simplified by removing the reference models in the smoothness terms. The rotation matrix between the two coordinate systems is

$$\mathbf{R} = \begin{pmatrix} \cos\theta & \sin\theta \\ -\sin\theta & \cos\theta \end{pmatrix}, \quad (5)$$

which can be applied to the horizontal and vertical derivatives of the model so that orthogonal derivatives in an arbitrary coordinate system can be obtained

$$\frac{\partial m}{\partial x'} = \cos\theta\frac{\partial m}{\partial x} + \sin\theta\frac{\partial m}{\partial z} \quad (6a)$$

$$\frac{\partial m}{\partial z'} = -\sin\theta\frac{\partial m}{\partial x} + \cos\theta\frac{\partial m}{\partial z}. \quad (6b)$$

Substitution of eq. (6) into eq. (4) provides the dipping model objective function

$$\phi_m(m) = \int_V w_s\left(m - m_{\text{ref}}\right)^2 dv + \int_V w_{x'}\left(\cos\theta\frac{\partial m}{\partial x} + \sin\theta\frac{\partial m}{\partial z}\right)^2 dv + \int_V w_{z'}\left(-\sin\theta\frac{\partial m}{\partial x} + \cos\theta\frac{\partial m}{\partial z}\right)^2 dv, \quad (7)$$

which rearranges to

$$\phi_m(m) = \int_V w_s\left(m - m_{\text{ref}}\right)^2 dv + \int_V \left(w_{x'}\cos^2\theta + w_{z'}\sin^2\theta\right)\left(\frac{\partial m}{\partial x}\right)^2 dv + \int_V \left(w_{x'}\sin^2\theta + w_{z'}\cos^2\theta\right)\left(\frac{\partial m}{\partial z}\right)^2 dv + \int_V 2\left(w_{x'} - w_{z'}\right)\cos\theta\sin\theta\frac{\partial m}{\partial x}\frac{\partial m}{\partial z}dv, \quad (8)$$

and the discrete representation is

$$\Phi_m = (\mathbf{m} - \mathbf{m}_{\text{ref}})^{\mathrm{T}}\mathbf{W}_s^{\mathrm{T}}\mathbf{W}_s(\mathbf{m} - \mathbf{m}_{\text{ref}}) + \mathbf{m}^{\mathrm{T}}\left(\mathbf{D}_x^{\mathrm{T}}\mathbf{B}_x\mathbf{D}_x + \mathbf{D}_z^{\mathrm{T}}\mathbf{B}_z\mathbf{D}_z + \mathbf{D}_x^{\mathrm{T}}\mathbf{B}_{xz}\mathbf{D}_z + \mathbf{D}_z^{\mathrm{T}}\mathbf{B}_{xz}\mathbf{D}_x\right)\mathbf{m}, \quad (9)$$

where $\mathbf{D}_x$ and $\mathbf{D}_z$ are finite difference operators; $\mathbf{B}_x$, $\mathbf{B}_z$, and $\mathbf{B}_{xz}$ are diagonal matrices containing the trigonometric terms in eq. (8); and the last term in eq. (8) is represented by two cross-terms in eq. (9) to promote symmetry.

Here, we use ℓ^2-norms (sum-of-squares) but note that general measures, such as those of Farquharson (1998), could be employed instead to encourage sharp interfaces. In that case, the objective function must remain in the form of eq. (7) before discretization because the form in eq. (8) is only valid for ℓ^2-norms.

2.4 Extension to 3-D: specification of strike, dip, and tilt

In the 3-D coordinate system let $+x$ be in the northing direction, $+y$ easting, and $+z$ down. Three angles are required to define the orientation of a 3-D planar object (i.e. a plate): φ is the strike angle (the intersection of the plane with a horizontal surface) defined positive east of north; θ is the dip defined positive downward from horizontal; and ψ is the tilt. Li & Oldenburg (2000) used a tilt instead of a plunge because the strike direction as defined previously is constant under arbitrary tilt angle. The graphic representation of the 3-D scenario as depicted in Li & Oldenburg (2000) is shown in Fig. 2. The tilt is the rotation of the object within its dipping plane around the y' axis in Fig. 2.

The 3-D rotation matrix is created via three sequential rotations. First, a rotation of φ is performed around the z axis. With $\varphi > 0$ this moves x towards y creating new axes x' and y' (refer to Fig. 2). The first rotation matrix is

$$\mathbf{R}_z = \begin{pmatrix} \cos\varphi & \sin\varphi & 0 \\ -\sin\varphi & \cos\varphi & 0 \\ 0 & 0 & 1 \end{pmatrix}. \quad (10)$$

This is followed by a rotation of $\theta - 90^\circ$ around the newly formed x' axis. With $0 < \theta < 90^\circ$ this moves z towards y' creating new axis z'. The second rotation matrix is

$$\mathbf{R}_x = \begin{pmatrix} 1 & 0 & 0 \\ 0 & \cos(\theta - 90) & \sin(\theta - 90) \\ 0 & -\sin(\theta - 90) & \cos(\theta - 90) \end{pmatrix} = \begin{pmatrix} 1 & 0 & 0 \\ 0 & \sin(\theta) & -\cos(\theta) \\ 0 & \cos(\theta) & \sin(\theta) \end{pmatrix}. \quad (11)$$

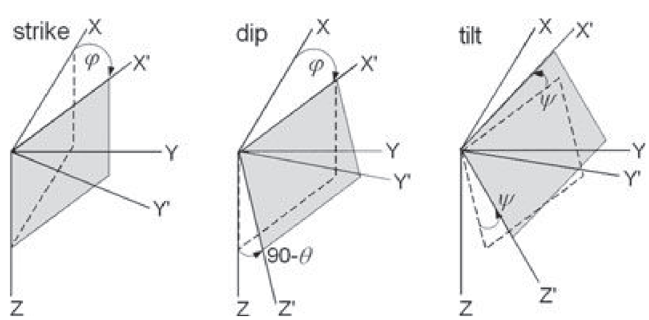

Figure 2. The mesh-orthogonal and rotated coordinate systems for a 3-D problem (this figure was reproduced from Li & Oldenburg 2000).

Finally, a rotation of ψ occurs around the y' axis. With $\psi > 0$ this moves x' towards z'. Note that there is an inconsistency in sign between this last rotation and that shown in Fig. 2 provided by Li & Oldenburg (2000). The third rotation matrix is

$$\mathbf{R}_y = \begin{pmatrix} \cos(-\psi) & 0 & -\sin(-\psi) \\ 0 & 1 & 0 \\ \sin(-\psi) & 0 & \cos(-\psi) \end{pmatrix} = \begin{pmatrix} \cos(\psi) & 0 & \sin(\psi) \\ 0 & 1 & 0 \\ -\sin(\psi) & 0 & \cos(\psi) \end{pmatrix}. \tag{12}$$

The final 3-D rotation matrix is created by combining those above

$$\mathbf{R} = \mathbf{R}_y\mathbf{R}_x\mathbf{R}_z = \begin{pmatrix} r_{xx} & r_{xy} & r_{xz} \\ r_{yx} & r_{yy} & r_{yz} \\ r_{zx} & r_{zy} & r_{zz} \end{pmatrix},$$

with

$$\begin{aligned} r_{xx} &= \cos\varphi\cos\psi - \sin\varphi\cos\theta\sin\psi \\ r_{xy} &= \sin\varphi\cos\psi + \cos\varphi\cos\theta\sin\psi \\ r_{xz} &= \sin\theta\sin\psi \\ r_{yx} &= -\sin\varphi\sin\theta \\ r_{yy} &= \cos\varphi\sin\theta \\ r_{yz} &= -\cos\theta \\ r_{zx} &= -\cos\varphi\sin\psi - \sin\varphi\cos\theta\cos\psi \\ r_{zy} &= -\sin\varphi\sin\psi + \cos\varphi\cos\theta\cos\psi \\ r_{zz} &= \sin\theta\cos\psi. \end{aligned} \tag{13}$$

Note that a typographical error in Li & Oldenburg (2000) provides an inconsistency in sign between the r_{zy} quantity in eq. (13) and that given in Li & Oldenburg (2000).

2.5 The choice of difference operators

The matrix multiplications and additions in eq. (9) indicate that the matrices $\mathbf{D}_x$ and $\mathbf{D}_z$ must be square and of the same size. In the non-rotated (mesh-aligned) formulation, the traditional discrete differential operators calculate differences across cell-faces, with the x-direction gradients defined on vertical cell faces and the z-direction gradients defined on horizontal cell faces. Consequently, $\mathbf{D}_x$ and $\mathbf{D}_z$ are never square and are only the same size if the mesh contains the same number of cells in all directions. Li & Oldenburg (2000) defined the discrete x and z gradients at the centres of each cell so that the difference operators are the same size.

For a 1-D problem with four model cells of unit dimensions (see Fig. 3) the traditional $\mathbf{D}_x$ operator would be

$$\mathbf{D}_x = \begin{pmatrix} -1 & 1 & 0 & 0 \\ 0 & -1 & 1 & 0 \\ 0 & 0 & -1 & 1 \end{pmatrix}, \tag{14}$$

which has three rows that define three differences operating across the three faces between the four cells. With differences defined at cell centres we need four differences (one for each cell) instead of three.

Figure 3. A 1-D mesh with four cells.

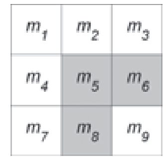

Figure 4. A 3×3 2-D mesh. The shaded cells indicate those involved in the finite differences defined at the centre of cell 5 when forward differences are employed.

2.5.1 *Cell-centred forward and backward differences*

One option is to use forward differences for all cells and backward differences where necessary:

$$\mathbf{D}_x = \begin{pmatrix} -1 & 1 & 0 & 0 \\ 0 & -1 & 1 & 0 \\ 0 & 0 & -1 & 1 \\ 0 & 0 & -1 & 1 \end{pmatrix}. \tag{15}$$

Forward differences are used for cells 1–3 in Fig. 3. A backward difference must be used for cell 4, which results in a difference operator with the lower two rows identical. This was the approach taken by Li & Oldenburg (2000). One may expect, as is shown below, that the use of backward differences instead may lead to different results.

Now consider a 3×3 package of cells in a 2-D model, as shown in Fig. 4. The x- and z-direction forward differences for the central cell 5 involve cells 6 and 8, respectively. Writing eq. (7) for only cell 5 yields

$$\begin{aligned} \phi_m(m) = {} & w_s\big(m_5 - m_{\mathrm{ref},5}\big)^2 dv \\ & + w_{x'}\big(\cos\theta(m_6 - m_5) + \sin\theta(m_8 - m_5)\big)^2 dv \\ & + w_{z'}\big(-\sin\theta(m_6 - m_5) + \cos\theta(m_8 - m_5)\big)^2 dv. \end{aligned} \tag{16}$$

With $\theta = +45^\circ$ this reduces to

$$\begin{aligned} \phi_m(m) = {} & w_s\big(m_5 - m_{\mathrm{ref},5}\big)^2 dv \\ & + w_{x'}\big(-2m_5 + m_6 + m_8\big)^2 dv \\ & + w_{z'}\big(m_8 - m_6\big)^2 dv. \end{aligned} \tag{17}$$

(a constant in the smoothness terms equal to $\cos 45^\circ = \sin 45^\circ$ has been ignored here for simplification purposes). To recover a model elongated in the new x' direction (which dips at $+45^\circ$) we would set $w_{x'} \gg w_{z'}$ and effectively have

$$\begin{aligned} \phi_m(m) = {} & w_s\big(m_5 - m_{\mathrm{ref},5}\big)^2 dv \\ & + w_{x'}\big(-2m_5 + m_6 + m_8\big)^2 dv. \end{aligned} \tag{18}$$

With $\theta = -45^\circ$, we would instead obtain

$$\begin{aligned} \phi_m(m) = {} & w_s\big(m_5 - m_{\mathrm{ref},5}\big)^2 dv \\ & + w_{x'}\big(m_6 - m_8\big)^2 dv \\ & + w_{z'}\big(-2m_5 + m_6 + m_8\big)^2 dv. \end{aligned} \tag{19}$$

and setting $w_{x'} \gg w_{z'}$ effectively gives

$$\begin{aligned} \phi_m(m) = {} & w_s\big(m_5 - m_{\mathrm{ref},5}\big)^2 dv \\ & + w_{x'}\big(m_6 - m_8\big)^2 dv. \end{aligned} \tag{20}$$

Note that there is an asymmetry indicated here: in eq. (18) (for $\theta = +45^\circ$) the x' term considers values in three cells, whereas in eq. (20) (for $\theta = -45^\circ$) the x' term contains only two cell values.

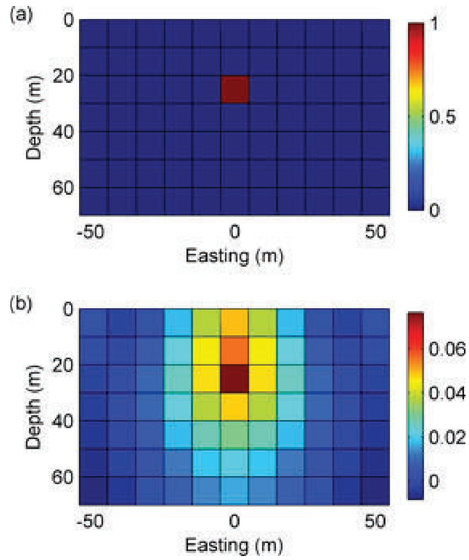

Figure 5. The true 2-D density model is in (a). The recovered 2-D density model with no preferred elongation direction specified ($w_{x'} = w_{z'} = 1.0$) is in (b).

This asymmetry of the forward (or backward) differences leads to asymmetric results.

To demonstrate the asymmetric effects we present a small 2-D gravity example. The true model is shown in Fig. 5(a), for which gravity data are modelled and a small amount of noise added before inverting. The smallness and smoothness weights are constant across the model; w_s is set to 0.001 to balance the smallness and smoothness terms and the smoothness weights are either 1.0 or 0.001 (depending on the inversion). We set the reference model equal to the true model and apply this reference model in the smallness term only; we do so to make the asymmetric effects more apparent in the figures presented. Fig. 5(b) shows the result of an inversion specifying no preferred elongation direction. The asymmetry of the forward differences is evident when comparing the result in

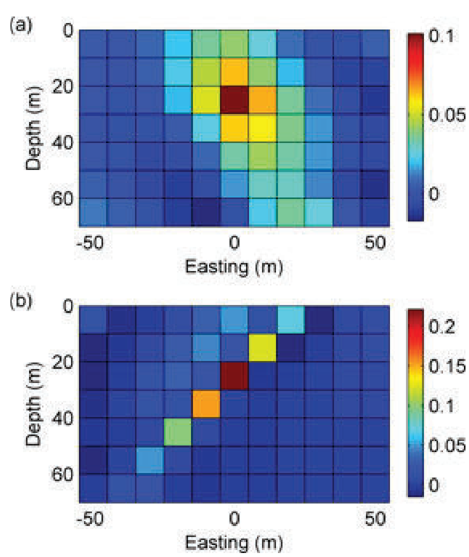

Figure 6. The recovered 2-D density models using a dipping-objective function with forward differences used in the model objective function. The specified dips are (a) $+45^\circ$ and (b) -45°. The weights used were $w_{x'} = 1.0$ and $w_{z'} = 0.001$ across the entire mesh.

Fig. 6(a), in which we specify $\theta = +45^\circ$, to that in Fig. 6(b), in which we specify $\theta = -45^\circ$. Ideally those two results should be symmetric across a vertical line bisecting the mesh (ignoring any asymmetry introduced by the random noise added to the data).

2.5.2 *Cell-centred long differences*

There are three options for promoting symmetry. The first is to use long differences across a cell. Consider again the 3×3 2-D package of cells in Fig. 4. Using long differences across cell 5 would provide the following contribution to the objective function in eq. (7)

$$\begin{aligned}\phi_m(m) = {} & w_s\left(m_5 - m_{\mathrm{ref},5}\right)^2 dv \\ & + w_{x'}\left(\cos\theta(m_6 - m_4) + \sin\theta(m_8 - m_2)\right)^2 dv \\ & + w_{z'}\left(-\sin\theta(m_6 - m_4) + \cos\theta(m_8 - m_2)\right)^2 dv. \end{aligned} \quad (21)$$

The result is that the even-numbered cells are all linked together through the finite-difference interactions in the model objective function, and similarly the odd-numbered cells are all linked together. However, no differences occur between even- and odd-numbered cells. In other words, each cell is linked through the difference operators to the cells diagonally adjacent to it, but there is no link to the cells across its faces. The mesh is, thereby, separated into two parts like a chessboard with a set of ‘black’ cells and a set of ‘white’ cells as in Fig. 7(a): all the black cells are linked to each other, and the same is true for the white cells, but none of the black cells are linked to any of the white cells. Hence, smoothness can be maintained in the diagonal directions but not in the axial directions.

Mathematically, the chessboard pattern in Fig. 7(a) is an annihilator for the discrete gradient operators formed using long differences. That is, given some model, we can arbitrarily add some value to all the ‘black’ model cells, and arbitrarily add some other value to all the ‘white’ model cells, and the value of the smoothness terms in the model objective function will not change (similarly, a constant value is also an annihilator for the smoothness terms). One might say that the chessboard pattern is invisible to the smoothness terms in the model objective function when long differences are used.

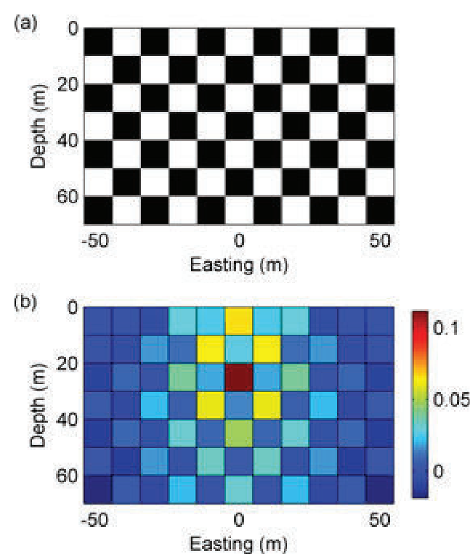

Figure 7. A chessboard pattern is in (a). The recovered 2-D density model using node-centred finite-difference operators in the model objective function with $\theta = 45^\circ$ and $w_{x'} = w_{z'}$ is in (b).

2.5.3 Node-centred integration

The second option for promoting symmetry is to move to a node-centred integration scheme. We would then use 2×2 packages of cells in 2-D. Consider the top left 2×2 package of cells in Fig. 4. A nodal scheme would integrate the model objective function around each node (rather than over each cell) such that the contribution to the model objective function for the node within the top left 2×2 package of cells would be

$$\begin{aligned}\phi_m(m) = &\ (\text{smallness terms})\\ &+ w_{x'}\big(\cos\theta(m_2 - m_1 + m_5 - m_4)\\ &\quad + \sin\theta(m_4 - m_1 + m_5 - m_2)\big)^2 dv\\ &\quad + w_{z'}\big(-\sin\theta(m_2 - m_1 + m_5 - m_4)\\ &\quad + \cos\theta(m_4 - m_1 + m_5 - m_2)\big)^2 dv.\end{aligned} \tag{22}$$

With $\theta = 45^\circ$ this reduces to

$$\begin{aligned}\phi_m(m) = &\ (\text{smallness terms})\\ &\quad + w_{x'}\left(m_5 - m_1\right)^2 dv\\ &\quad + w_{z'}\left(m_4 - m_2\right)^2 dv.\end{aligned} \tag{23}$$

At first glance this may seem appropriate, with diagonal differences as requested by setting $\theta = 45^\circ$. However, note that the chessboard annihilator again becomes an issue. In Fig. 7(b), we show the result of inverting the example gravity data with a node-centred scheme, specifying $\theta = 45^\circ$ and with $w_{x'} = w_{z'}$. The chessboard annihilator pattern is clearly visible.

2.5.4 Four quadrant face-centred integration

Our solution for discretization avoids asymmetric results and the chessboard annihilator. We follow the traditional approach of calculating derivatives through finite differences across cell faces. In 2-D, the elemental areas in which the *x*- and *z*-directional differences are defined are on different overlapping grids, as indicated in Fig. 8. Hence, we must split each cell into four quadrants as indicated in Fig. 8 and integrate over each quadrant separately. In quadrant 5d the *x*-direction difference is between the values in cells 6 and 5, and the *z*-direction difference is between the values in cells 8 and 5: this is much like using forward differences in quadrant 5d. In quadrant 5a, we would essentially use backward differences for both the *x*- and *z*-directions; in quadrants 5b and 5c, we would use a mixture of forward and backward differences. Hence, this approach is equivalent to using four sets of $\mathbf{D}_x$ and $\mathbf{D}_z$ operators, each set using a different option for the differences (forward or backward) as indicated in Table 1.

Let the i^{th} operators be denoted $\mathbf{D}_{x,i}$ and $\mathbf{D}_{z,i}$. The discrete representation of our 2-D model objective function is

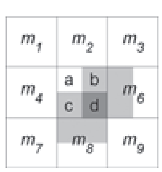

Figure 8. A 3×3 2-D mesh. The central cell 5 is split into 4 quadrants. The shaded regions across cell faces indicate the regions across which *x*- and *z*-direction forward finite differences are calculated for cell 5 (those regions overlap in quadrant 5d).

Table 1. Difference options for the four sets of finite difference operators for the 2-D dipping model objective function.

set	$\mathbf{D}_x$	$\mathbf{D}_z$
1	Backward	Backward
2	Forward	Backward
3	Backward	Forward
4	Forward	Forward

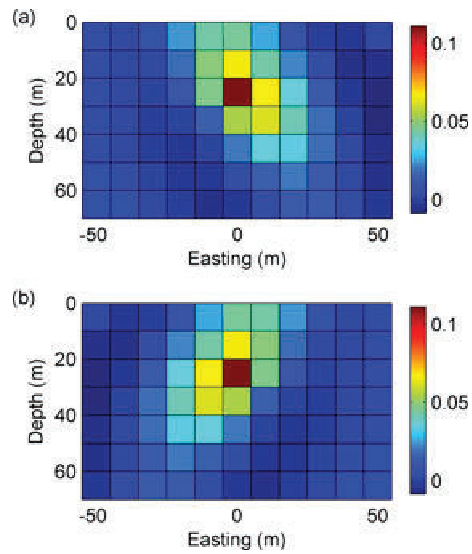

Figure 9. The recovered 2-D density models using a dipping-objective function with four sets of differences used in the model objective function. The specified dips are (a) +45° and (b) −45°. The weights used were $w_{x'} = 1.0$ and $w_{z'} = 0.001$ across the entire mesh.

then

$$\begin{aligned}\Phi_m = &\ (\mathbf{m} - \mathbf{m}_{\text{ref}})^{\mathrm{T}}\mathbf{W}_s^{\mathrm{T}}\mathbf{W}_s(\mathbf{m} - \mathbf{m}_{\text{ref}})\\ &+ \mathbf{m}^{\mathrm{T}}\frac{1}{4}\sum_{i=1}^{4}\big(\mathbf{D}_{x,i}^{\mathrm{T}}\mathbf{B}_x\mathbf{D}_{x,i} + \mathbf{D}_{z,i}^{\mathrm{T}}\mathbf{B}_z\mathbf{D}_{z,i}\\ &+ \mathbf{D}_{x,i}^{\mathrm{T}}\mathbf{B}_{xz}\mathbf{D}_{z,i} + \mathbf{D}_{z,i}^{\mathrm{T}}\mathbf{B}_{xz}\mathbf{D}_{x,i}\big)\,\mathbf{m}\\ = &\ (\mathbf{m} - \mathbf{m}_{\text{ref}})^{\mathrm{T}}\mathbf{W}_s^{\mathrm{T}}\mathbf{W}_s(\mathbf{m} - \mathbf{m}_{\text{ref}}) + \mathbf{m}^{\mathrm{T}}\mathbf{W}^{\mathrm{T}}\mathbf{W}\mathbf{m},\end{aligned} \tag{24}$$

which yields a $\mathbf{W}^{\mathrm{T}}\mathbf{W}$ operator that provides symmetric results (i.e. the results do not depend on the sign of θ) as is evident from comparing the results in Fig. 9. Returning to the 2-D example of Fig. 4, the central cell 5 is now linked to all the cells across its faces, as indicated by the shaded cells in Fig. 10. The chessboard issue is also ameliorated using this four set approach. In 3-D, we use eight sets of operators (all possible permutations).

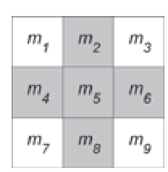

Figure 10. A 3×3 2-D mesh. The shaded cells indicate those involved in the finite differences defined at the centre of cell 5 when four sets of finite difference operators are employed.

2.6 Specifying orientations at point locations

The smoothness weights $w_{x'}$ and $w_{z'}$ can be homogeneous across the entire mesh or can be set to different values in different regions. It is, thereby, possible to specify orientations globally or locally. Li & Oldenburg (2000) elected to specify orientations on a regional basis. Instead, we extend the functionality such that different orientations can be specified at each mesh cell centre. Of course, orientations involve spatial gradients across finite distances so to say that we allow specification of an orientation at a point in space is somewhat misleading; in our formulation, each cell is linked to the cells adjacent to it so the cell-based orientations are, thereby, spread out to influence surrounding cells and the overlap inherent here acts as a smoothing mechanism.

2.7 A practical issue: depth and distance weighting

Depth weighting, or a more general distance weighting, must be incorporated into gravity and magnetic inversions due to the fall-off of the responses with distance. In Li & Oldenburg (1996, 1998), a depth weighting function $Z(z)$ is applied to the model such that the model objective function is of the form

$$\begin{aligned}\phi_m(m) = &\int_V w_s\big(Z(z)(m - m_{\mathrm{ref}})\big)^2 dv\\ &+ \int_V w_x\left(\frac{\partial Z(z)m}{\partial x}\right)^2 dv\\ &+ \int_V w_y\left(\frac{\partial Z(z)m}{\partial y}\right)^2 dv\\ &+ \int_V w_z\left(\frac{\partial Z(z)m}{\partial z}\right)^2 dv.\end{aligned} \tag{25}$$

Here, the depth weighting is applied inside the derivatives of the smoothness terms. The discrete representation would be

$$\Phi_m = \|\mathbf{W}_s\mathbf{Z}(\mathbf{m} - \mathbf{m}_{\mathrm{ref}})\|^2 + \cdots + \|\mathbf{D}_z\mathbf{Z}\mathbf{m}\|^2. \tag{26}$$

This approach had proven to work satisfactorily on a number of synthetic examples and became the default choice in the algorithm of Li & Oldenburg (1996).

There is an issue here, however. With the depth weighting applied inside the derivatives, the z-smoothness term no longer provides an exact z-direction gradient because the model is altered by the depth weighting before the differential operator is applied. With depth weighting, this is only an issue for the z-direction since in the other smoothness terms the order of operations is irrelevant (i.e. Z is a function of z only and can, therefore, be taken outside of the derivatives with respect to x and y). With distance weighting, however, all smoothness terms are affected. It would be more appropriate to perform the depth or distance weighting outside the derivatives such that the model objective function is of the form

$$\begin{aligned}\phi_m(m) = &\int_V w_s Z_s(z)^2\big(m - m_{\mathrm{ref}}\big)^2 dv\\ &+ \int_V w_x Z_x(z)^2\left(\frac{\partial m}{\partial x}\right)^2 dv\\ &+ \int_V w_y Z_y(z)^2\left(\frac{\partial m}{\partial y}\right)^2 dv\\ &+ \int_V w_z Z_z(z)^2\left(\frac{\partial m}{\partial z}\right)^2 dv.\end{aligned} \tag{27}$$

where we have added subscripts to the depth weighting matrices to indicate that they may be of different sizes. The discrete representation would be

$$\Phi_m = \|\mathbf{Z}_s\mathbf{W}_s(\mathbf{m} - \mathbf{m}_{\mathrm{ref}})\|^2 + \cdots + \|\mathbf{Z}_z\mathbf{D}_z\mathbf{m}\|^2. \tag{28}$$

The issue is especially important when using a rotated objective function: if depth weighting is applied inside the z-derivative then the derivative calculated is not the exact z-gradient quantity required.

3 INCORPORATING ORIENTATION INFORMATION AS HARD CONSTRAINTS

Specifying elongation information (i.e. axis directions and aspect ratios) through the smoothness measures is considered a soft constraint: we request of the inversion that the specified elongations be recovered but there is no guarantee. To obtain such a guarantee we can include the orientation information as hard constraints by bounding spatial model gradients and gradient ratios. We now consider two scenarios. In the first, we investigate how to bound the direction of the spatial gradient. In the second, we consider how to specify a physical property increase or decrease along a particular direction.

3.1 Bounding the spatial gradient direction

Let l and u specify lower and upper bounds on the dip angle θ: in 2-D we can then write the trigonometric inequalities

$$\tan l \leq \left(\tan\theta = \frac{\nabla_z m}{\nabla_x m}\right) \leq \tan u. \tag{29}$$

After discretization, eq. (29) gives

$$\mathbf{L}\mathbf{D}_x\mathbf{m} \leq \mathbf{D}_z\mathbf{m} \leq \mathbf{U}\mathbf{D}_x\mathbf{m} \tag{30}$$

where $\mathbf{L}$ and $\mathbf{U}$ are diagonal matrices containing the bounding values on their main diagonals. To simplify, we can split eq. (30) into two inequalities

$$\mathbf{D}_z\mathbf{m} \geq \mathbf{L}\mathbf{D}_x\mathbf{m} \tag{31a}$$

$$\mathbf{U}\mathbf{D}_x\mathbf{m} \geq \mathbf{D}_z\mathbf{m} \tag{31b}$$

which rearrange to

$$(\mathbf{D}_z - \mathbf{L}\mathbf{D}_x)\mathbf{m} \geq \mathbf{0} \tag{32a}$$

$$(\mathbf{U}\mathbf{D}_x - \mathbf{D}_z)\mathbf{m} \geq \mathbf{0} \tag{32b}$$

and lead to linear constraints of the form

$$\mathbf{A}\mathbf{m} \geq \mathbf{b}. \tag{33}$$

Eq. (33) is a system of equations, each of the form

$$a_1 m_1 + a_2 m_2 + \cdots \geq b. \tag{34}$$

These constraints can be added to the inverse problem such that the resulting optimization problem is

$$\min_{\mathbf{m}} \quad \Phi_d(\mathbf{m}) + \beta\Phi_m(\mathbf{m}) \tag{35a}$$

$$\text{s.t.} \quad \mathbf{A}\mathbf{m} \geq \mathbf{b}. \tag{35b}$$

In 3-D we could write more trigonometric inequalities for the three angles φ, θ, and ψ. However, the resulting inequalities no longer reduce to linear constraints. For example, with $\psi = 0$ and $\varphi \neq 0$ the 3-D equivalent to eq. (29) is

$$\tan l \leq \left(\tan\theta = \frac{\nabla_z m}{\sqrt{(\nabla_x m)^2 + (\nabla_x m)^2}} \right) \leq \tan u, \tag{36a}$$

and the squaring leads to non-linear inequalities. Such constraints would increase the difficulty of the optimization problem and for this reason we do not consider them further.

3.2 Specifying directions of increase or decrease

We now re-pose the problem by specifying that a directional spatial derivative, in some specified location and direction $\vec{v}$, lies between some bounds. The directional derivative is the dot product of $\vec{v}$ with the spatial model gradient. In 3-D, we obtain the inequality

$$l \leq \left(v_x \nabla_x + v_y \nabla_y + v_z \nabla_z \right) m \leq u \tag{37}$$

where the lower and upper bounds l and u can be used to specify that the physical property increases, decreases or remains constant along the direction $\vec{v}$. The discrete form is

$$\mathbf{L} \leq \left(\mathbf{V}_x \mathbf{D}_x + \mathbf{V}_y \mathbf{D}_y + \mathbf{V}_z \mathbf{D}_z \right) \mathbf{m} \leq \mathbf{U} \tag{38}$$

where matrices $\mathbf{L}$, $\mathbf{U}$, $\mathbf{V}_x$, $\mathbf{V}_y$, and $\mathbf{V}_z$ are diagonal. Again, eq. (38) can be reduced to the simple form in eq. (33).

3.3 Practical application of linear constraints

In eqs (30) and (38), we again have a situation in which the difference operators must be the same size. We can take the same approach as in Section 2.5 and use four sets of operators, and therefore, four sets of linear inequalities (or eight in 3-D). This issue is removed if we simplify the problem to placing bounds on a particular gradient component, for example

$$\mathbf{L} \leq \mathbf{D}_z \mathbf{m} \leq \mathbf{U}, \tag{39}$$

or to specifying some other general relationship between model parameters, for example

$$a_1 m_1 + a_2 m_2 + \cdots \geq b. \tag{40}$$

Consider a situation in which we can say with some certainty that one region of the subsurface is one rock type, another region is a second rock type, but we are not sure which of the two rock types falls between those two regions. Perhaps one rock type is an intrusion into the second, or perhaps the two units are separated by an offset fault at depth. Another possible scenario involves a cover unit of unknown thickness above another unit. If relative physical property values between rock types are known then model gradient values can be bounded in the unknown region. With less confident physical property information we may still be able to specify the sign of the model gradients in the unknown region (i.e. specifying a directional increase or decrease).

The linear constraints developed above allow specification of relative spatial relationships between rock units. They also allow incorporation of information regarding the direction and magnitude of alteration gradients. Another use is to incorporate poorly calibrated physical property measurements taken on rock samples, in which case the values could only be treated as relative (i.e. $l \leq m_1/m_2 \leq u$).

3.4 Linear inequality constrained inverse problems

Earlier we indicated how orientation information can be specified in a hard manner through the addition of linear constraints to the optimization problem. We now present a strategy for solving the inverse problem with linear inequality constraints. To minimize the problem in eq. (35), we follow the approach of Li & Oldenburg (2003) and use a logarithmic barrier method. Although there are modern alternatives to the logarithmic barrier method (refer to Gill 1995), it has proven to be a feasible solution method for large 3-D geophysical inversion problems with simple bound constraints. The extension to linear constraints is as follows. The logarithmic barrier method adds a barrier term Φ_λ to the objective function and solves a sequence of unconstrained inversions

$$\min_{\mathbf{m}} \quad \Phi(\mathbf{m}) - \lambda \Phi_\lambda(\mathbf{m}) \tag{41}$$

while carefully cooling the value of λ. The barrier term is

$$\Phi_\lambda = \sum_{i=1}^{M} \log\left(\mathbf{a}_i^{\mathrm{T}} \mathbf{m} - b_i \right) \tag{42}$$

$$= \mathbf{e}^{\mathrm{T}} \log\left(\mathbf{A}\mathbf{m} - \mathbf{b} \right) \tag{43}$$

where $\mathbf{e}$ is a vector of ones, $\mathbf{a}_i^{\mathrm{T}}$ is the ith row of $\mathbf{A}$ and the log operation on a vector quantity is element-by-element.

We use a Newton-type descent method to solve the unconstrained subproblem, and therefore, we require the first and second order derivatives (the gradient and Hessian) of the logarithmic barrier term. The gradient is

$$\mathbf{g}_\lambda = \left(\frac{d\Phi_\lambda}{d\mathbf{m}} \right)^{\mathrm{T}} \tag{44}$$

$$= \left(\mathbf{e}^{\mathrm{T}} \frac{\partial \log(\mathbf{y})}{\partial \mathbf{y}} \frac{d\mathbf{y}}{d\mathbf{m}} \right)^{\mathrm{T}} \Bigg|_{\mathbf{y}=\mathbf{A}\mathbf{m}-\mathbf{b}} \tag{45}$$

$$= \left(\mathbf{e}^{\mathrm{T}} diag\left(\mathbf{y}^{-1} \right) \mathbf{A} \right)^{\mathrm{T}} \tag{46}$$

$$= \mathbf{A}^{\mathrm{T}} diag\left(\mathbf{y}^{-1} \right) \mathbf{e} \tag{47}$$

$$= \mathbf{A}^{\mathrm{T}} \mathbf{y}^{-1}, \tag{48}$$

where the power operation on $\mathbf{y} = \mathbf{A}\mathbf{m} - \mathbf{b}$ is element-by-element. The Hessian is

$$\mathbf{H}_\lambda = \frac{d\mathbf{g}_\lambda}{d\mathbf{m}} \tag{49}$$

$$= \mathbf{A}^{\mathrm{T}} \frac{\partial \left(\mathbf{y}^{-1} \right)}{\partial \mathbf{y}} \frac{d\mathbf{y}}{d\mathbf{m}} \tag{50}$$

$$= -\mathbf{A}^{\mathrm{T}} diag\left(\mathbf{y}^{-2} \right) \mathbf{A}. \tag{51}$$

Once a step direction $\boldsymbol{\delta}\mathbf{m}$ is chosen we will update the current (k^{th}) model with

$$\mathbf{m}^{(k+1)} = \mathbf{m}^{(k)} + \alpha \boldsymbol{\delta}\mathbf{m}, \tag{52}$$

where the step length α is determined by performing a line search. We need to determine the maximum step length possible α_{max} without violating the constraints. For each linear constraint, we have

$$\mathbf{a}_i^{\mathrm{T}} \mathbf{m} \geq b_i, \tag{53}$$

and we want to know the value α_i, such that

$$\mathbf{a}_i^{\mathrm{T}} (\mathbf{m} + \alpha_i \boldsymbol{\delta}\mathbf{m}) = b_i$$
$$\mathbf{a}_i^{\mathrm{T}} \mathbf{m} + \alpha_i \mathbf{a}_i^{\mathrm{T}} \boldsymbol{\delta}\mathbf{m} = b_i$$
$$\alpha_i = \left(b_i - \mathbf{a}_i^{\mathrm{T}} \mathbf{m}\right) / \left(\mathbf{a}_i^{\mathrm{T}} \boldsymbol{\delta}\mathbf{m}\right). \quad (54)$$

If the result for α_i is negative then the search direction will not violate the i^{th} constraint regardless of the positive step length. Hence, we must calculate the α_i value for every linear constraint and take the smallest positive value of those as the limiting value $\alpha_{\max}$. We then set

$$\alpha = \min(\alpha_{\max}, 1.0). \quad (55)$$

Practical aspects of our algorithm follow Li & Oldenburg (2003). The step length is reduced slightly to ensure that we stay off the barrier

$$\mathbf{m}^{(k+1)} = \mathbf{m}^{(k)} + \gamma \alpha \boldsymbol{\delta}\mathbf{m}, \quad \gamma = 0.925. \quad (56)$$

The barrier parameter is updated as

$$\lambda^{(k+1)} = [1 - \min(\alpha, \gamma)] \, \lambda^{(k)} \quad (57)$$

and the barrier iterations are continued until the barrier term has a negligible contribution to the total objective function.

The logarithmic barrier method is an interior-point method, meaning that the iterates remain feasible (the model always satisfies the constraints). This is required to avoid taking the logarithm of a negative number. The major practical difficulty is then that the initial model must be feasible and for complicated linear inequalities the creation of a feasible initial model may be a difficult task. We emphasize that these types of constrained optimization problems are at the leading edge of optimization research and future advances in that field may lead to more advantageous solution methods.

3.5 Applying hard orientation constraints to a two-dimensional example

We now return to the small 2-D gravity example in Section 2.5 and add linear inequality constraints into the problem such that we specify a dip of $\theta = 45^\circ$ around the cell containing the anomalous density in the true model. The most thorough way to proceed would be to write eq. (32) for that cell. This would be done for each four sets of permutations in Table 1 and would result in eight linear inequality constraints involving the cell of interest and its neighbours. Although that is possible, we continue with a more simple demonstration and create two pairs of linear constraints, each pair linking the cell of interest to one of its diagonally adjacent cells. If the cell of interest corresponds to cell 5 in Fig. 4, then the linear constraints we use here specify

$$-0.001 \le m_5 - m_1 \le 0.001 \quad (58a)$$

$$-0.001 \le m_5 - m_9 \le 0.001 \quad (58b)$$

(i.e. cells 1 and 9 should contain values close to that in cell 5). We perform the same inversion that lead to the result in Fig. 9(a) but apply the constraints in eq. (58). The recovered model, shown in Fig. 11, honours the linear inequality constraints in eq. (58) and the $+45^\circ$ dip is clearly evident.

Alternatively, without some knowledge of the expected value in the cells being constrained, we may wish to specify that the relative change between two cells be less than some value, say 5 per cent.

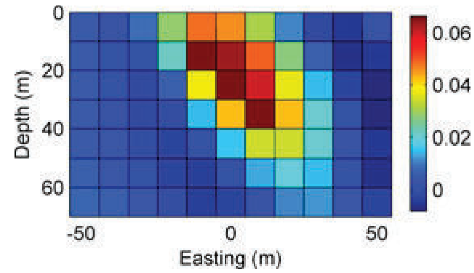

Figure 11. The recovered 2-D density model from a similar inversion to that for Fig. 9(a) but with additional linear inequality constraints in eq. (58) added into the inversion.

This would lead to constraints of the form

$$-0.05 \le \frac{m_5 - m_1}{m_1} \le 0.05$$
$$-0.05 m_1 \le m_5 - m_1 \le 0.05 m_1, \quad (59)$$

which for this example would yield similar results.

4 INCORPORATING DIFFERENT FORMS OF ORIENTATION INFORMATION

As mentioned in the introduction, orientation information may come in different forms. We now demonstrate our methods for including different forms of orientation information on a more complicated 2-D magnetics example. The true model, shown in Fig. 12(a), represents a scenario in which a layered sequence of rock units has been folded into a syncline. The uniform discrete mesh is 47 cells × 23 cells. Magnetic data are calculated for the true model and a small amount of noise is added before inverting. We set the noise level below the amplitude of the signal from the lowest portion of the lower susceptible layer. The inversions are thus provided a chance to recover the lower susceptible layer but, as will become evident, the non-uniqueness of the problem makes it difficult to recover the layered scenario unless further geological information (e.g. orientation information) is incorporated into the problem.

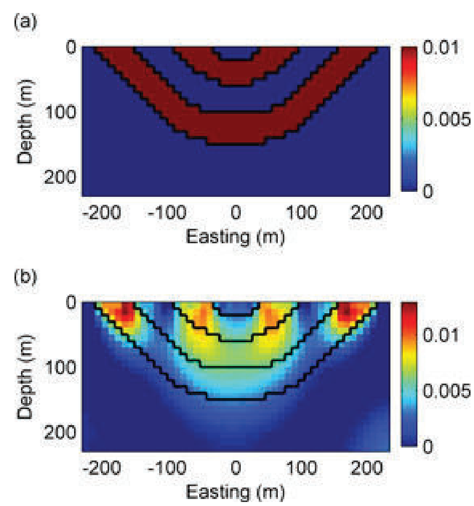

Figure 12. The true 2-D susceptibility model is in (a). The recovered 2-D susceptibility model with no preferred elongation direction specified ($w_x = w_z = 1.0$) is in (b). The location of the layers in the true model are indicated with a thick black line in (b).

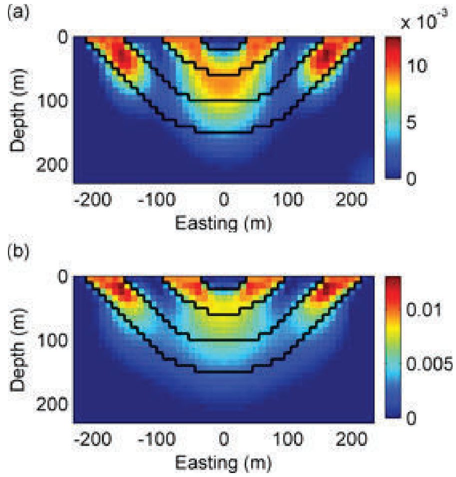

Figure 13. The recovered 2-D susceptibility models with the following information incorporated into the inversions: (a) surface bounds; (b) surface bounds and surface orientations.

For all inversions mentioned below, the reference model is set to zero; smallness weights w_s are set to zero to emphasize the effects of incorporating orientation information. Fig. 12(b) shows the inversion result with no preferred elongation direction specified ($w_x = w_z = 1.0$). This inversion fails to adequately resolve the two magnetic layers and places significant susceptible material where there is none in the true model.

4.1 Incorporating surface orientation information

Surface mapping can provide direct local measurements of structural orientation. We now assume that surface mapping has provided physical property measurements and orientations at the surface, which we can incorporate into the inversion. We set the susceptibility bounds across the surface equal to the true values $\pm 5.0 \times 10^{-4}$, which corresponds to 5 per cent of the true value of the susceptible layers. The result with surface bounds included is in Fig. 13(a).

In a real scenario we would need to make a decision on how deep to extend the orientation information. Here we take the approach of pushing the orientations to depth but weighting those orientations higher near the surface: this is done by setting $w_{x'}/w_{z'} = 100$ (where x' is in the along-dip direction) at the surface and decreasing that ratio to unity (i.e. no preferred elongation direction) at depths greater than five cells (50 m). The result is shown in Fig. 13(b). Incorporating the surface orientation information improves the result slightly. The upper susceptible layer is better recovered but the model still does not clearly indicate the presence of two magnetic layers at depth.

4.2 Incorporating interpreted volumetric orientation information

After surface mapping, subsequent drilling may allow interpretation of approximate orientations across larger volumes. Assuming that a drill-hole has been placed vertically through the centre of the model to a depth of 190 m, we may then make an interpretation of a synclinal structure and develop a preliminary model of the subsurface dip as shown in Fig. 14(a).

Without further investigation we would want to limit the weighting on those interpreted orientations as there is less confidence in them than for the measured orientations. We include the interpreted

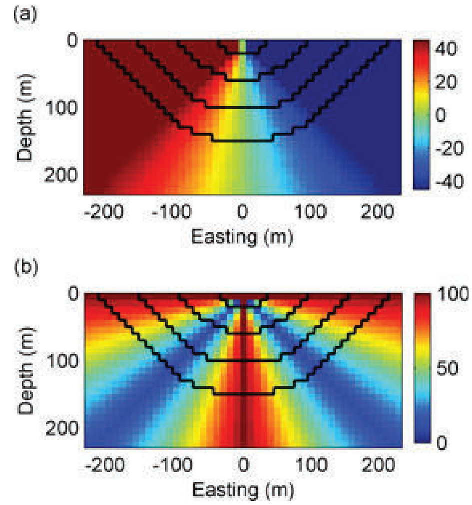

Figure 14. Interpreted dips (angles in degrees) for the 2-D synclinal model are in (a). The $w_{x'}/w_{z'}$ ratios used across the volume for the result in Fig. 15(b) are in (b).

dip information in Fig. 14(a) and set $w_{x'}/w_{z'} = 100$ near the surface and drill-hole location but decrease the ratio to 10.0 away from those locations to provide a lower weighting on the interpreted dips where we have less confidence. The $w_{x'}/w_{z'}$ ratios used across the volume are shown in Fig. 14(b).

We also assume that the drill-core is logged with physical property measurements allowing us to include bounds in the cells along the drill-hole (we again set the bounds equal to the true susceptibility values $\pm 5.0 \times 10^{-4}$). Furthermore, we note that in previous inversions there has been a tendency to put higher susceptibility close to the surface. Hence, we limit the maximum susceptibility to be 0.0105 (the same as the largest upper bound for the surface and drill-hole cells).

The result with only the surface and drill-hole bounds (i.e. no orientation information) is in Fig. 15(a). The result with the interpreted volumetric orientation information incorporated is in Fig. 15(b). Incorporating this orientation information clearly improves the result and now indicates the presence of two distinct magnetic layers.

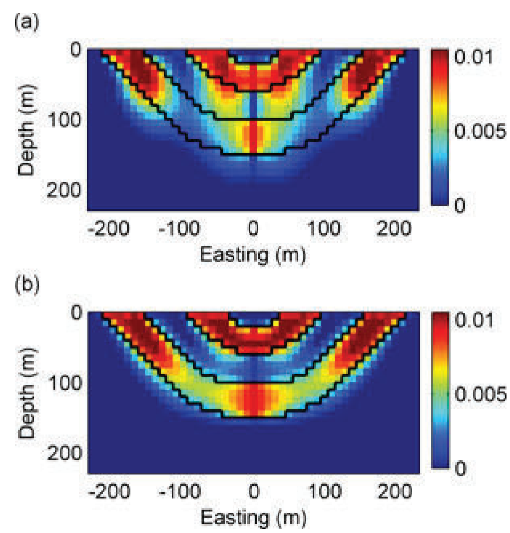

Figure 15. The recovered 2-D susceptibility models with the following information incorporated into the inversions: (a) surface and drill-hole bounds; (b) surface and drill-hole bounds, and interpreted orientations at depth.

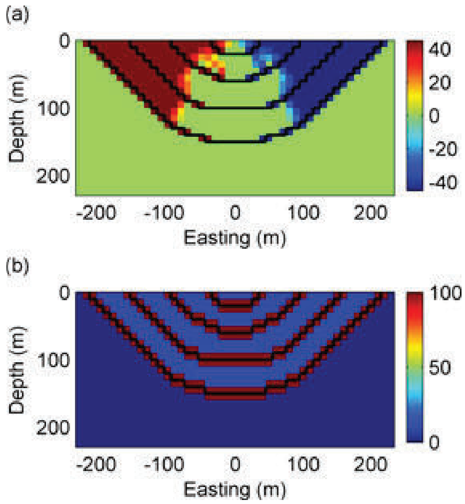

Figure 16. Calculated and interpolated dips (angles in degrees) for the 2-D synclinal rock model are in (a). Cells where dip cannot be calculated or interpolated (i.e. below the bottom-most susceptible layer) have been set to zero. The $w_{x'}/w_{z'}$ ratios used across the volume for the result in Fig. 17(a) are in (b).

4.3 Incorporating orientation information from a rock model

Even without explicit physical property values attached, a geological (rock) model still contains valuable orientation information. In this final iteration, we assume that a geological model has been created in the later stages of exploration. Assuming that this model confidently locates the interfaces between the true rock units, we can calculate orientations associated with the interfaces and assign those orientations to the cells adjacent to the interfaces. We can then interpolate orientations in cells between the interfaces. The resulting orientations for our syncline example are shown in Fig. 16(a).

We set $w_{x'}/w_{z'}$ to a high value (=100) in cells adjacent to the interfaces, to a lower value (=10.0) where dips have been interpolated between interfaces, and to unity elsewhere. The $w_{x'}/w_{z'}$ ratios used across the volume are shown in Fig. 16(b). If the geological knowledge for a particular scenario leads us to believe that there are gradational physical property changes (i.e. not sharp interfaces) between rock units then this can be specified by decreasing the $w_{x'}/w_{z'}$ ratio closer to unity.

The inversion result with orientation information from the rock model incorporated is shown in Fig. 17(a). The layers are well recovered, as expected since the rock model contains the true interface locations.

An alternative or additional strategy is to add linear constraints to the problem. We now add additional linear constraints of the form in eq. (59)

$$-0.1m_j \le m_i - m_j \le 0.1m_j, \tag{60}$$

which specifies a relative difference of 10 per cent between the values in cells i and j. Between the easting coordinates -25 m and $+25$ m we specify that cells horizontally adjacent to each other should obey eq. (60) (i.e. the information along the drill-hole trace is extended out horizontally). To the west of -95 m and to the east of $+95$ m we expect features that dip at $+45°$ and $-45°$, respectively, and we therefore specify that the diagonally adjacent cells along those dip directions should obey eq. (60). The result with these

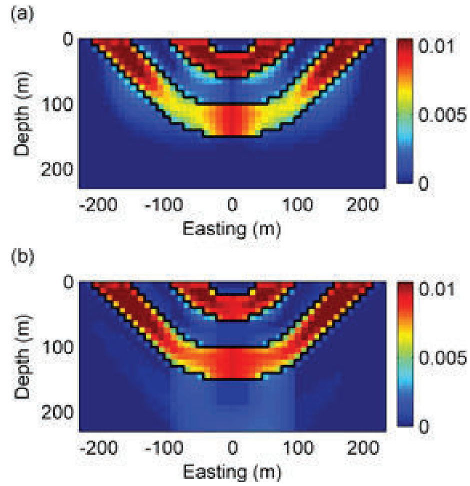

Figure 17. The recovered 2-D susceptibility models with surface and drill-hole bounds, and interface location information incorporated into the inversions. The inversion for (a) had bound constraints only. Additional linear constraints were incorporated for (b).

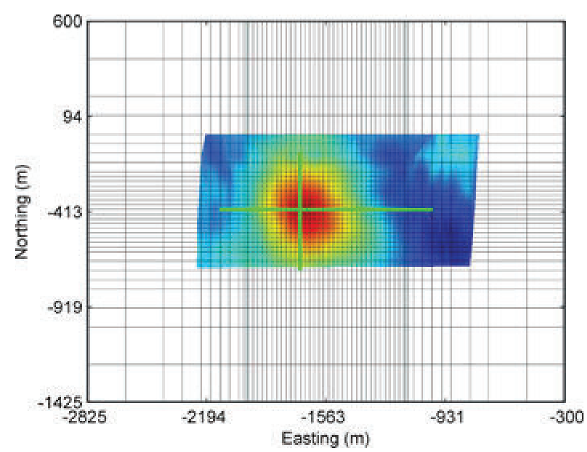

Figure 18. A top view of the mesh used to invert the San Nicolás gravity data, a map of which is overlayed. The mesh has 53×33×35 cells (easting–northing-depth). The locations of the cross-sections shown in the figures that follow are indicated with green lines.

linear constraints is shown in Fig. 17(b), which provides further improvement.

5 APPLICATION TO THE SAN NICOLÁS DEPOSIT

Phillips (2001) performed considerable work on geophysical data from the San Nicolás massive sulphide copper–zinc deposit (Zacatecas, Mexico). Here, we apply our methods to the gravity data therein. The inversion mesh is shown in Fig. 18 and the data are plotted in Figs 18 and 19(a). There is a detailed geological model available, interpreted from an extensive drilling program, that we can use to constrain the inversions. Our first step is to create a density model from the geological model and the physical property information available. That model is shown in Fig. 20; the high density sulfide body is evident (red in those images). The deposit is bounded to the east by a southwest-dipping fault. Mineralization continues along the fault to depth to create a smaller keel structure that is evident on the left of Figs 20(a) and (b).

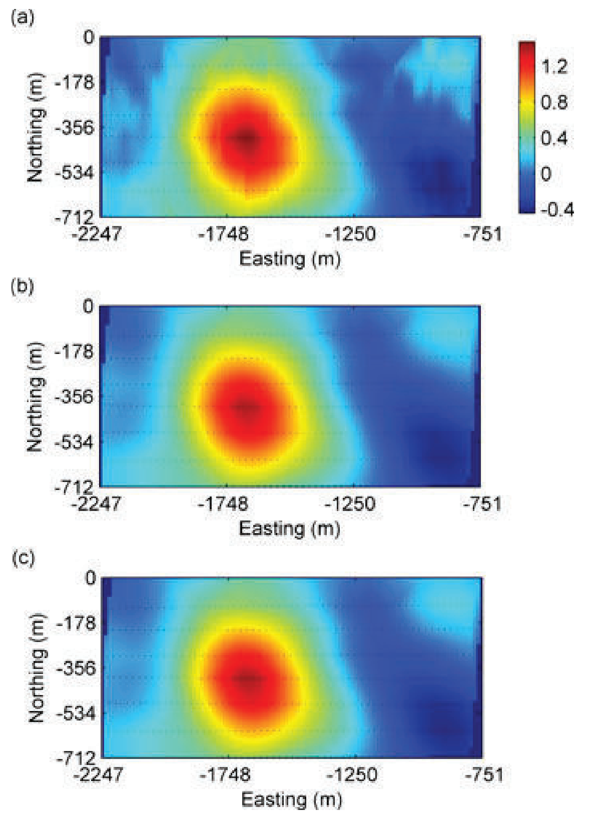

Figure 19. A map of the San Nicolás gravity data (mGal) is in (a); a regional component has been removed from the original data used in Phillips (2001). The predicted data for the model in Fig. 22 is in (b). The predicted data for the model in Fig. 23 is in (c). All three data maps are plotted on the same scale for comparison. The locations of the 422 data are indicated by black dots.

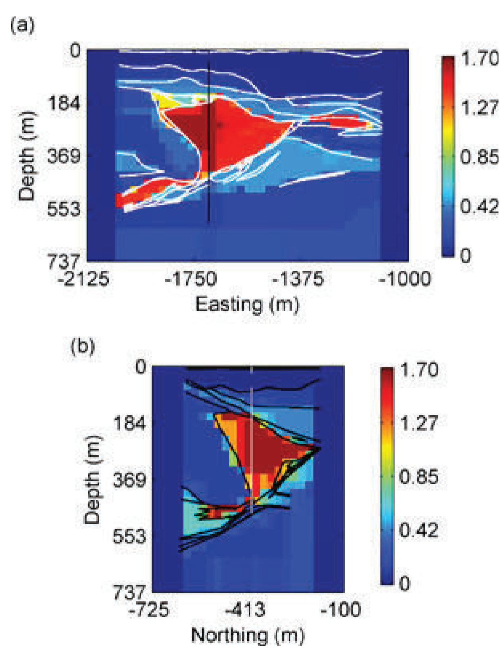

Figure 20. The anomalous density model (g cc^{-1}) created from the geological model and physical property information for the San Nicolás deposit: (a) shows a W–E cross-section at northing $= -400$ m; (b) shows a S–N cross-section at easting $= -1700$ m. Interfaces in the geological model are outlined in white for the W–E section and in black for the S–N section.

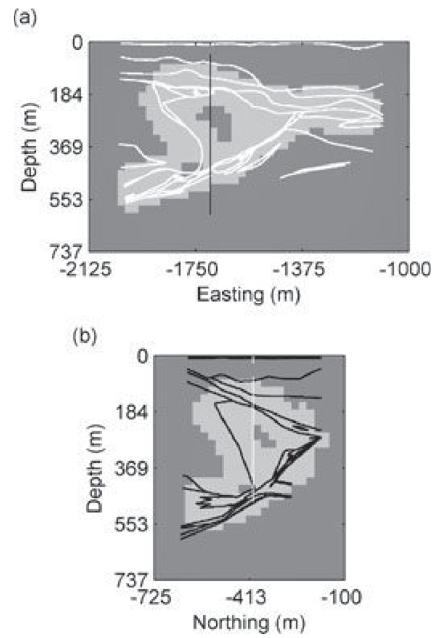

Figure 21. The $w_{x'}$ smoothness weights used in the inversion of the San Nicolás data with orientation information incorporated: (a) shows a W–E cross-section at northing $= -400$ m; (b) shows a S–N cross-section at easting $= -1700$ m. Interfaces in the geological model are outlined in white for the W–E section and in black for the S–N section. Weights of 1.0 are shown in dark grey and weights of 0.01 are shown in light grey.

We next calculate the spatial model gradient in each cell for the model in Fig. 20. High values of the gradient amplitude will occur where the interfaces in the geological model exist (i.e. between rock units). Where the gradient amplitude is above some threshold we incorporate orientation information. The threshold value is determined by looking at isosurfaces and finding a threshold value for which the isosurface defines a fully connected set of interfaces for the main sulphide body and the keel. We use the orientation of the gradient vectors to specify rotation angles such that we can align one axis normal to, and two axes tangential to, the planar interfaces in the geological model. If the x' axis is normal to an interface then we set $w_{x'} = 0.01$ and $w_{y'} = w_{z'} = 1.0$ to encourage the inversion to place sharp jumps in density across (normal to) the interface and maintain smoothness along (tangential to) the interface. Fig. 21 indicates where the orientation information is applied (i.e. where the $w_{x'}$ smoothness weights are set low).

Figs 22 and 23 show cross-sections through recovered models obtained through inversions without and with orientation information incorporated, respectively. The predicted data for those models are shown in Fig. 19. The recovered model with orientation information incorporated better emphasizes the distinct high density sulphide body by placing sharp density jumps across the interfaces.

Due to corrections applied and regional components removed during data processing steps, it is difficult to compare the density values from the geological model with those in the inversion results in an absolute sense. We can, however, compare the range of density values in the models (i.e. maximum value minus minimum value). Another issue is that forward modelling for the density model in Fig. 20 (from the geological model) creates a response with a range of approximately twice that of the observed data (see Fig. 24). The density range for the geological model is 1.70 (g cc^{-1}), but considering the forward modelling results, a value of 0.85 is a

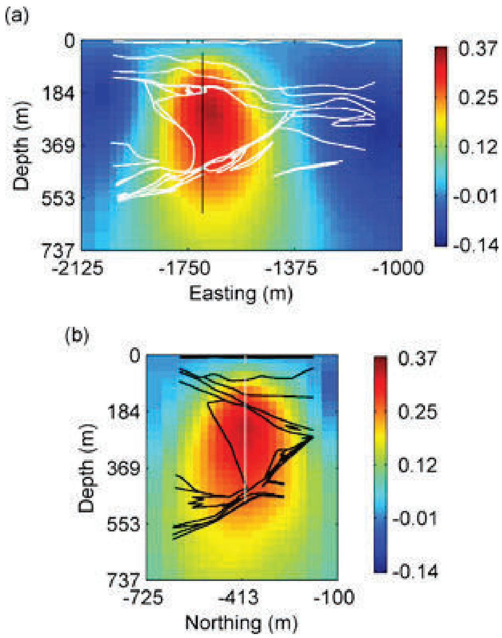

Figure 22. The recovered density model (g cc^{-1}) for the default, unconstrained inversion of the San Nicolás data: (a) shows a W–E cross-section at northing = −400 m; (b) shows a S–N cross-section at easting = −1700 m. Interfaces in the geological model are outlined in white for the W–E section and in black for the S–N section.

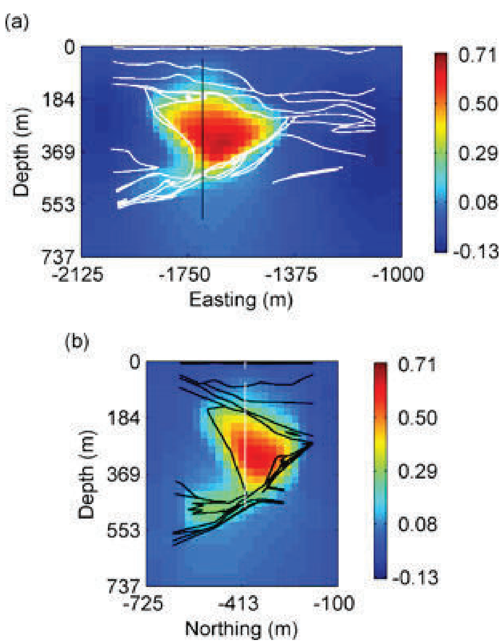

Figure 23. The recovered density model (g cc^{-1}) for the inversion of the San Nicolás data with orientation information incorporated: (a) shows a W–E cross-section at northing = −400 m; (b) shows a S–N cross-section at easting = −1700 m. Interfaces in the geological model are outlined in white for the W–E section and in black for the S–N section.

better value to compare with our results. The unconstrained result has a density range of 0.51 compared to 0.84 for the constrained result. Hence, the constrained result provides significantly improved density estimates.

In the unconstrained result, there is no indication of the keel. In the constrained result, there is a density structure recovered where

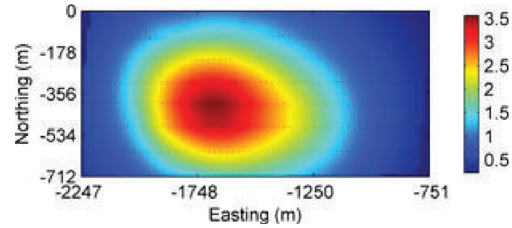

Figure 24. A map of the gravity data (mGal) forward modelled for the model in Fig. 20. The locations of the 422 data are indicated by black dots.

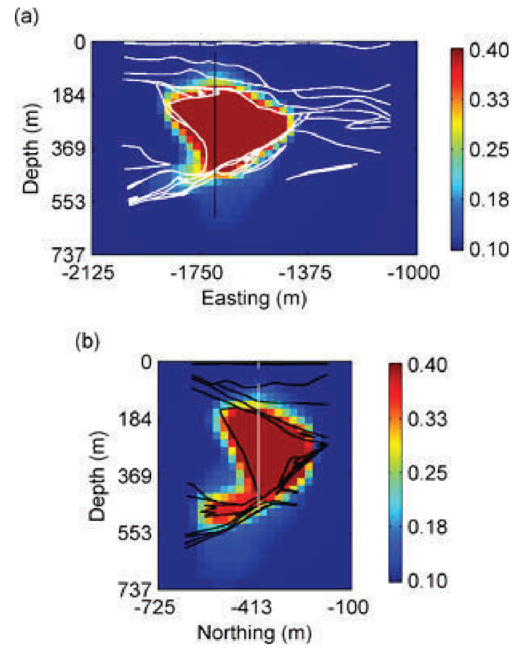

Figure 25. This figure shows the same information as in Fig. 23 but the colour scale has been altered to better emphasize the keel structure at depth.

the keel is expected to lie; this is most evident in Fig. 25(b). The keel is difficult to model due to two factors. First, forward modelling experiments in Phillips (2001) showed that the gravity response of the keel is expected to lie only slightly above the estimated noise level for the data. Hence, there is only minimal data support for the keel and we cannot expect the inversions to recover this deep structure well. Second, the discretization used results in mesh cells that are larger than some smaller spatial dimensions of the keel. If an inversion on this mesh happens to recover a structure indicative of the keel, we would expect upscaling of the keel structure onto the larger mesh cells to cause lower densities than expected (i.e. a small, high density structure becomes a larger, lower density structure once averaged onto a larger volume). This explains the lowered recovered density for the keel in the constrained result.

6 APPLICATION TO THE HISLOP DEPOSIT

Mitchinson (2009) applied geophysical inversion to the Hislop gold deposit (eastern Timmins, Ontario, Canada) to help target Archean orogenic gold mineralization. Here we apply our methods to the magnetic data therein. The inversion mesh is shown in Fig. 26 and the data is plotted in Figs 26 and 27(a). The Hislop deposit is hosted within a structurally complicated area, characterized by numerous faults and tight folds. Some larger faults define the edges of a

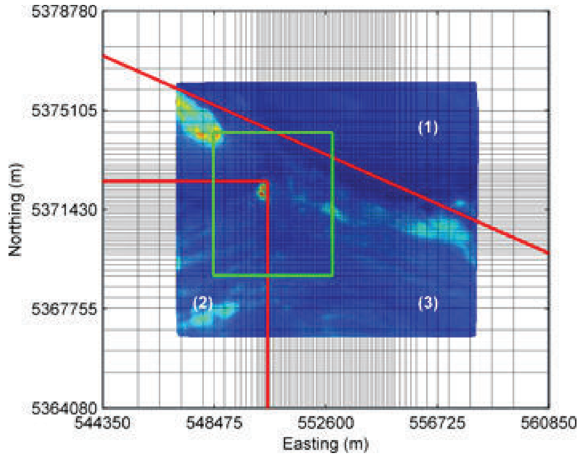

Figure 26. A top view of the mesh used to invert the Hislop magnetic data, a map of which is overlayed. The mesh has 73 × 55 × 40 cells (easting–northing-depth). Three regions are numbered and their boundaries indicated with red lines. The outline of the volumes shown in Fig. 28 is indicated with a green rectangle.

Table 2. Strike and dip values (degrees) assigned to each region indicated in Fig. 26.

Region	Strike	Dip
1	115	80
2	71	90
3	115	90

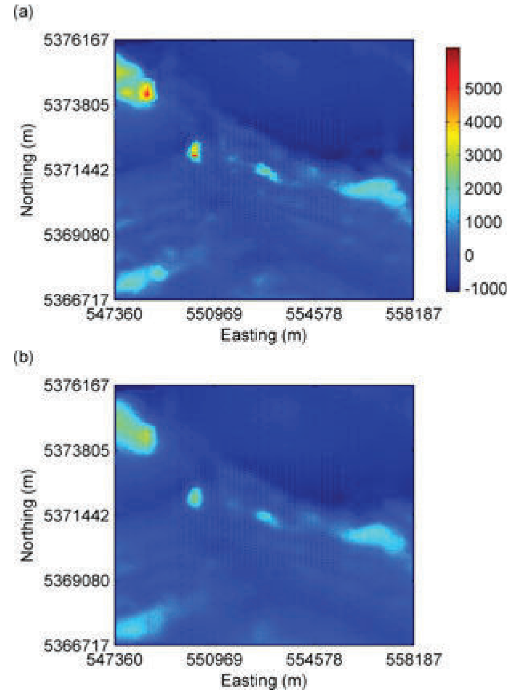

Figure 27. A map view of the Hislop magnetic data is shown in (a). The predicted data for the model in Fig. 28(a) are in (b). The predicted data map for the model in Fig. 28(b) is visibly indistinguishable from that in (b) so we do not show it. Both data maps are plotted on the same scale for comparison. The locations of the 1725 data are indicated by black dots.

high susceptibility region consisting of Fe-rich mafic and ultramafic volcanic rocks (VUO). Gold tends to occur in proximity to faults, making them important structural aspects of the subsurface.

Knowledge of the area has lead geologists to expect elongated tabular features that are steeply dipping and strike in different directions in different regions of the subsurface. Three regions are indicated in Fig. 26 and Table 2 gives the strike and dip values assigned to each region. This information is used to rotate the smoothness directions across the inversion mesh. The smoothness weights are set to $w_{x'} = w_{z'} = 1$ and $w_{y'} = 0.01$ over the entire inversion volume to encourage tabular features that extend in the strike (x') and dip (z') directions. The recovered models without and with this information incorporated into the inversions are shown in Figs 28(a) and (b), respectively. The predicted data for those models are shown in Fig. 27(b). The most obvious difference between the two recovered models is the change in shape of the highest susceptibility feature at centre, which becomes laterally more narrow once orientation information is incorporated. Another significant difference is the orientation of a lower susceptibility near-surface feature to the south of that body, which dips towards the south in Fig. 28(a) but is nearly vertical in Fig. 28(b).

Two large faults of interest are indicated in Fig. 28, the depth traces of each having been interpreted from the recovered susceptibility models. Most gold deposits in the area are focused along the regional crustal-scale Porcupine-Destor Fault (shown in white in Fig. 28); knowledge of its location and orientation is important for understanding the regional geology and tectonics, and for focusing exploration programs. The local fault (which has no offical name; shown in black in Fig. 28) is where the majority of the gold is localized at the Hislop site; understanding its orientation and extent has implications on subsequent drill-hole spotting and mine planning.

The two interpretations for the depth trace of the local fault show different dip, especially closer to the surface. This indicates that more geological information needs to be gathered (e.g. via drilling) to validate one interpretation or the other. One could also carry out more inversions with different local orientations and weights to assess what orientations of the local fault are reasonable from a data perspective. In contrast, the interpreted depth traces of the Porcupine-Destor Fault are similar, suggesting that this consistent depth trace is required by the data and providing confidence in the interpretation. The magnetic inversions have been helpful in mapping the Porcupine-Destor Fault location to depths below the limits of drilling.

7 CONCLUSION

Incorporating orientation information into geophysical inversions can significantly improve the results, especially for gravity and magnetic problems, which have poor resolution at depth, and we have provided a comprehensive look at the available methods for including this information. We have improved upon the work of Li & Oldenburg (2000) for including structural orientation information in geophysical inversions by developing a finite difference scheme for the numerical derivatives which ameliorates problems of asymmetry evident in the original implementation. We have also developed an approach that relies on additional linear constraints placed in the optimization problem.

ACKNOWLEDGMENTS

We are grateful to Dr Yaoguo Li for discussions regarding this work; Teck Corporation for providing the San Nicolás data; Nigel Phillips

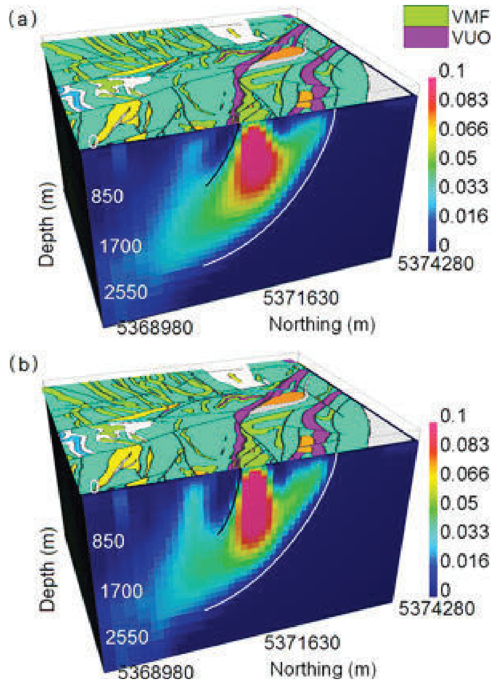

Figure 28. Vertical cross-sections at easting = 552 850 m through the susceptibility models recovered from inversion of the Hislop data. The default, unconstrained inversion result is shown in (a). The result with orientation information incorporated is shown in (b). A geological map, adapted from an interpretation by Power *et al.*, unpublished data, has been overlayed on top of the mesh: the legend on top right in (a) indicates the colours of the magnetic mafic volcanic rocks (VMF) and VUO. Interpreted depth traces for two faults are indicated with white and black lines: the Porcupine-Destor Fault is white and the local fault (no official name) black.

for his help inverting the San Nicolás data; St. Andrew Goldfields Ltd., for providing the Hislop data; and Dr Dianne Mitchinson for her help inverting and interpreting the Hislop data, and her contributions to the text of that section. This manuscript was significantly improved by reviews from Dr Michel Chouteau and Dr Antonio Guillen.

REFERENCES

Barbosa, V.C.F. & Silva, J.B.C., 1994. Generalized compact gravity inversion, *Geophysics,* **59,** 57–68.

Barbosa, V.C.F. & Silva, J.B.C., 2006. Interactive 2D magnetic inversion – a tool for aiding forward modeling and testing geological hypotheses, *Geophysics,* **71,** L43–L50.

Bosch, M., Guillen, A. & Ledru, P., 2001. Lithologic tomography – an application to geophysical data from the Cadomian belt of Northern Brittany, France, *Tectonophysics,* **331,** 197–227.

Chasseriau, P. & Chouteau, M., 2003. 3D gravity inversion using a model of parameter covariance, *J. appl. Geophys.,* **52,** 59–74.

Farquharson, C.G. & Oldenburg, D.W., 1998. Non-linear inversion using general measures of data misfit and model structure, *Geophys. J. Int.,* **134,** 213–227.

Gill, P., Murray, W. & Wright, M., 1995. *Practical Optimization,* Academic Press, London.

Guillen, A., Calcagno, Ph., Courrioux, G., Joly, A. & Ledru, P., 2008. Geological modelling from field data and geological knowledge. Part II. Modelling validation using gravity and magnetic data inversion, *Phys. Earth planet. Int.,* **171,** 158–169.

Guillen, A. & Menichetti, V., 1984. Gravity and magnetic inversion with minimization of a specific functional, *Geophysics,* **49,** 1354–1360.

Last, B.J. & Kubik, K., 1983. Compact gravity inversion, *Geophysics,* **48,** 713–721.

Li, Y. & Oldenburg, D.W., 1996. 3-D inversion of magnetic data, *Geophysics,* **61,** 394–408.

Li, Y. & Oldenburg, D.W., 1998. 3D inversion of gravity data, *Geophysics,* **63,** 109–119.

Li, Y. & Oldenburg, D.W., 2000. Incorporating geologic dip information into geophysical inversions, *Geophysics,* **65,** 148–157.

Li, Y. & Oldenburg, D.W., 2003. Fast inversion of large-scale magnetic data using wavelet transforms and a logarithmic barrier method, *Geophys. J. Int.,* **152,** 251–265.

Mitchinson, D.E., 2009. Targeting Archean orogenic gold mineralization using physical properties and integrated geophysical methods, *PhD thesis*, University of British Columbia, Canada.

Mosegaard, K. & Tarantola, A., 2002. Probabilistic approach to inverse problems, *Int. Geophys.,* **81,** 237–265.

Phillips, N.D., 2001. Geophysical inversion in an integrated exploration program—examples from the San Nicolás deposit, *Master's Thesis,* University of British Columbia, Canada.

Wijns, C. & Kowalczyk, P., 2007, Interactive geophysical inversion using qualitative geological constraints, *Exploration Geophys.,* **38,** 208–212.